Materials
Advances

ROYAL SOCIETY
OF CHEMISTRY

PAPER

View Article Online
View Journal | View Issue

Cite this: *Mater. Adv.*, 2026, 7, 1153

# Optical studies of stimuli-responsive organic crystals differing in the position and nature of functional groups

Sumeera Farooq, Ishtiyaq Ahmad and Aijaz A. Dar *

Stimuli-responsive organic materials with dynamically configurable luminescence represent a transformative class of materials with far-reaching implications for next-generation sensing, secure data encryption, and high-performance display technologies. The scope of optical tuning and the ability to precisely modulate emission properties in response to external stimuli offer opportunities for the development of cutting-edge materials that enable breakthroughs in real-time detection, adaptation, and intelligent photonic devices. Focusing on the rational design of luminescent solids, we report three Schiff bases obtained by condensation of hydroxy naphthaldehyde with *para*-arsenate aniline [**1**, $\lambda_{max}$ 558 nm], *ortho*-arsenate aniline [**2**, $\lambda_{max}$ 525 nm], and *ortho*-sulfonate aniline [**3**, $\lambda_{max}$ 535 nm], differing in the position and nature of arsenate and sulfonate functional groups. Anticipated variation of optical properties in the new solid forms is triggered by variation in intra- and intermolecular factors. Structural studies reveal that solid-state emission arises due to the absence of any significant face-to-face $\pi$-stacking interactions, while emission tuning is realised through molecular electronic effects generated by functional groups. Multi-stimuli responsive studies carried out for **1–3** indicate the occurrence of crystallization-induced enhanced emission (CIEE) as the emission intensities decline in amorphous grounded forms, the observation further supported by thin film studies. Molecular solids **1** and **3** also exhibit reversible thermofluorochromism, arising due to breathing of lattice water in **3** and phase changes in non-solvated crystals of **1**. A non-emissive methanolic solution of **2** exhibits highly selective sensing for Zn(II) ions with an LOD value of $4.9 \times 10^{-6}$ M.

Received 21st September 2025,
Accepted 2nd December 2025

DOI: 10.1039/d5ma01080b

rsc.li/materials-advances

## Introduction

The advancement of next-generation fluorescent organic materials is propelling a rapidly expanding field with transformative applications in optoelectronics, high-performance sensors, seamless communications, and cutting-edge displays.[1–5] These innovations are driving breakthroughs in materials science, enabling unprecedented sensitivity, efficiency, and versatility across diverse technological domains. Schiff bases represent one of the simplest important classes of organic materials with a scope of facile functional group modification, unlocking new understanding and applications.[6–9] Incipience of solid-state luminescence and its tuning in these materials can be realised through the introduction of suitable functional groups and by changing their nature and positions in a molecule, as they influence electronic structure, molecular conjugation, and intermolecular interactions.[10–12] Besides, by tuning the HOMO–LUMO energy gaps, the functional groups can promote intramolecular charge transfer, enhancing photostability and solubility, which are critical for applications in biosensing, optoelectronics, and photonic materials.[13–15] Simple molecular modifications enable the design of materials with tailored optical and electronic functionalities, expanding their potential for development of cheaper next-generation sensors and displays.[16–18] Additionally, specific functional groups can promote excited-state proton transfer (ESIPT), aggregation-induced emission (AIE), or mechanofluorochromism and thermochromism, broadening their applicability as stimuli-responsive materials.[19–23]

Crystal engineering essentially involves understanding of the structure–property relationship in crystalline materials and the realisation of desired functions through crystal packing. Differences in the functional groups can establish intermolecular interactions differently, regulating crystal packings, which may also be affected by different positions of the same functional group (crystallochromism).[24–26] External crystallization factors like solvent polarity, temperature, *etc.*, can further influence the crystal packing in flexible organic

---

*Crystal Engineering Laboratory, Department of Chemistry, University of Kashmir, Hazratbal, Srinagar-190006, Jammu & Kashmir, India.
E-mail: aijazku2015@gmail.com, daraijaz@uok.edu.in*

molecules (polymorphism), resulting in modulated optical and physicochemical properties and catalytic efficiencies.[27,28]

The crystal engineering approaches involving functionalisation and co-crystallisation are therefore beneficial to realise tunable properties in organic molecules as they provide economical and benign alternatives to their inorganic counterparts.[29] For example, recently, metal-free Schiff bases have emerged as promising candidates for solid-state emission. Chuang Xie *et al.* developed optical waveguide materials using Schiff bases *via* a self-assembly approach.[30] Pance Naumov *et al.* explored their mechanical properties and correlations with optical behaviour to design flexible optical waveguides.[31,32] Soumyajit Ghosh *et al.* investigated the mechanical properties of different forms of anthracene Schiff base crystals, providing insights into their structural and functional characteristics.[33] Additionally, Emmerling *et al.* explored polymorph tuning in organic molecular crystals to optimize mechanical properties, leading to the development of flexible optical waveguide materials.[34] We have reported ON/OFF emission switching and multi-stimuli responsive behaviour in Schiff base triggered by polymorphism and crystallochromism.[35–37] These advancements highlight the immense potential of Schiff bases in emissive organic materials, providing new pathways for designing high-performance optoelectronic devices.

In this work, Schiff bases **1–3** were designed to optimize the supramolecular assembly through hydrogen bonding and charge transfer interactions, Scheme 1. We included structurally related arsenic acid and sulfonic acid groups in the π-conjugated scaffolds because of their good electron-withdrawing capability, to achieve molecular systems with varied electron density on two ends. Besides, the two types of functional groups can create a difference in crystal packing through variation in the hydrogen bonding pattern and result in different solid-state properties. Additionally, the position of the arsenic group was varied to understand the impact of the position of the group on molecular, crystal and material properties. Together with simultaneous exploration of the impact of variation and the position of functional groups, this work provides an opportunity to study the optical properties of organo-arsenates *vis-à-vis* their sulfonate counterparts. Through this study, we have realized notable solid-state emission tuning by changing the nature and position of functional groups, which, however, is more remarkable for positional isomers and retained in their thin film forms. Mechanochromism, thermochromism, and solvent-dependent emission of thin film forms are reported and compared. The results indicate the scope of organo-arsenates as a promising class of AIE materials with the CIEE tendency.

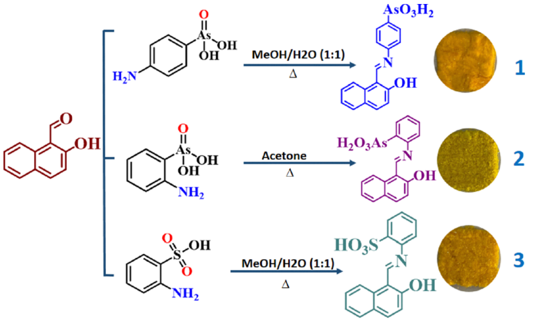

Scheme 1 Synthetic routes and bulk optical images of **1–3**.

## Experimental section

### Methods and materials

2-Aminophenylarsonic acid (98% TCI), 4-aminophenylarsonic acid (Sigma Aldrich), 2-aminobenzenesulfonic acid (95% Sigma Aldrich), and 2-hydroxy-1-naphthaldehyde (Sigma Aldrich) were utilised without further purification. Distilled methanol, acetone, and water were used for the Schiff base reactions and crystallization. Melting points were determined on the MP70 melting point system capillary apparatus (Mettler Toledo) in closed-end capillaries. Infrared spectroscopic data of products were recorded using a 630 FT-IR (4000–400 $cm^{-1}$) in ATR mode. Crystals of the products are placed on the crystal plate of the infrared instrument to record the spectrum. NMR ($^1H$) data were collected on a Joel JNM/ECZ 500R/S1 500 MHz spectrometer with an auto sampler facility. Mass analysis was carried out on a Xevo G2-XS QToF 4k (LC MS/MS) high resolution mass spectrometer with an Acquity H-Class PLUS UPLC system; *m*/*z*: 100 000. Thermal gravimetric analysis (TGA) of the products was performed on a simultaneous thermal analyzer-STA (LINSEIS, USA, 6807/8835/16) using an alumina crucible at a heating rate of 10 °C.

### Powder X-ray diffraction

The molecular solids were evaluated for phase purity and crystallinity by carrying out powder X-ray diffraction on a Bruker-AXS-D8-Advance diffractometer, recorded at room temperature. The samples were scanned in reflection mode over the $2\theta$ range of 25–50° with a step size of 0.02° at a scan rate of 8° $min^{-1}$.

### Single crystal X-ray diffraction (SC-XRD)

Single-crystal data were collected on a Rigaku Saturn 724+ CCD diffractometer using a graphite monochromator (Mo Kα, $\lambda$ = 0.71073 Å). The selected crystals were mounted on the tip of a glass pin using mineral oil, and the temperature of the crystal was maintained using nitrogen flow. Complete hemispheres of data were collected using $\omega$ and $\varphi$ scans (0.3°, 16 s per frame). Integrated intensities were obtained using Rigaku Crystal Clear-SM Expert 2.1 software, and they were corrected for absorption correction. Structure solution and refinement were performed using the SHELX package. The structures were solved by direct methods and completed by iterative cycles of $\Delta F$ syntheses and full-matrix least-squares refinement against $F$. Molecular structures and packing diagrams of crystal structures were plotted in Diamond with assistance from Mercury. The crystallographic data are summarized in Table S1.

### Hirshfeld (HS) analysis and 2D-fingerprint plots

Hirshfeld surface (HS) analysis and 2D fingerprint plot analysis were carried out using Crystal Explorer 17.5 software. Color-coding mapped on the $d_{\text{norm}}$ surface represents those contacts that indicate short (red), intermediate (white), and long contacts (blue) compared to the sum of van der Waals interactions. Hirshfeld surfaces were generated and mapped with the $d_{\text{norm}}$ function with a very high resolution. The electrostatic potential surface maps were generated in Crystal Explorer using the TONTO module within Crystal Explorer, with Hirshfeld surfaces mapped *via* Hartree–Fock theory (STO-3G basis set) over a range of −0.0030 to +0.0030 a.u. This approach highlights charge distribution and interaction sites on the molecular surface.

### Diffuse reflectance studies

Solid-state absorption studies have been carried out on the Shimadzu DRUV-2600 instrument using $BaSO_4$ discs. The HOMO and LUMO can be calculated by using the Kubelka–Munk function. Hence, the Kubelka–Munk equation at any wavelength can be written as:

$$K/S = (1 - R_\infty)^2/2R_\infty = F(R_\infty)$$

where $R_\infty$ is the diffuse reflectance and $F(R_\infty)$ is called the Kubelka–Munk function.

The Tauc relation for a direct HOMO LUMO of the material is given by the expression:

$$(\alpha h\nu) = A(h\nu - E_g)^n$$

where $\alpha$ is the linear absorption coefficient, $\upsilon$ is the light frequency, and $A$ is the proportionality constant. The power of the parentheses, $n$, is taken equal to $\frac{1}{2}$ for direct band gap materials.

### Fluorescence measurements

All the emission spectra were recorded at 25° ± 0.1 °C unless otherwise stated using an Agilent Cary Eclipse Fluorescence Spectrophotometer with slit widths of 5/5 and 5/2.5 (excitation/emission). To obtain Pl-spectra, all solid-phase fluorescence measurements were performed at an excitation wavelength of 365 nm.

### Stimuli-responsive studies

Mechanochromic studies of **1–3** were carried out by grinding the crystals in a mortar and pestle in a controlled manner, followed by diffuse reflectance and emission spectroscopy.

Thermochromic studies of **1–3** were followed by using emission spectroscopy. Initial screening was performed by taking a few milligrams of the compound on a glass slide that was kept on a heating mantle, having a temperature sensor with high precision and efficient temperature control, until a change in the color of the compounds was observed, and the fluorochromism was validated in a UV-visible chamber. Reversible thermochromism of **3** has further been validated by allowing **3H** form to cool under anhydrous conditions, created by storing it in a vail packed with activated silica, which was activated in an oven at 80–100 °C, for a week.

### Thin film studies

Thin films were formed in various solvents by making the slurry of compounds (concentration 5 mg $mL^{-1}$) in a given solvent, followed by drop casting on quartz slides. Spin coating was carried out to make uniform films at around 3000 rpm for 30 seconds, which were studied for their fluorescence behaviour.

### Sensing studies

A stock solution of **2** and solution of zinc acetate of concentration ($10^{-3}$ M) were prepared in methanol. 2 mL of the solution of **2** was titrated by incremental addition of metal ion solution until there was no increase in fluorescence intensity. Fluorescence spectra were recorded by selecting the excitation wavelength of 365 nm using an Agilent Cary Eclipse fluorescence spectrophotometer.

Furthermore, for the interference study, 2 mL of solution of **2** has been titrated with Zn(II) and other metal ion solutions ($10^{-3}$ M), prepared in tap water.

The detection limit is determined based on the fluorescence titration. The detection limit (LOD) of **2** for $Zn^{2+}$ is determined using the following equation.

$$\text{Detection limit (LOD)} = 3\sigma/k$$

where $\sigma$ represents the standard deviation and $k$ is the slope of the calibration curve.

For determining the stoichiometry of the metal ligand complex, Job's (continuous variation) plot was constructed by mixing equimolar concentrations of compound **2** and Zn(II) while varying the mole fraction of Zn(II) and **2** ($\chi$ = 0.0–1.0) and keeping the total concentration constant ($C_{\text{total}} = 1 \times 10^{-4}$ M). And for calculating the binding constant, the Benesi–Hildebrand equation was used.

### Synthesis of 1

4-Aminophenylarsonic acid (217 mg, 1 mmol) and 2-hydroxy-1-naphthaldehyde (173 mg, 1 mmol) were dissolved separately in 10 mL of methanol/$H_2O$ (1 : 1 v/v) and 10 mL of methanol, respectively, and then mixed. The resultant solution was stirred at 70 °C for 15–20 minutes and filtered hot to yield yellowish crystals in 20 minutes after slow evaporation. Yield: 65.0%. M.P: >250 °C. IR, $\nu$, $cm^{-1}$: 3100, 1626, 1367, 1099, 824. Abs. Peaks (nm): 407.$^1$H NMR (500 MHz, DMSO-$d_6$): 9.63 (s, 1H), 8.52–8.50 (d, 1H), 7.96–7.94 (d, 1H), 7.87–7.86 (m, 4H), 7.79–7.78 (m, 1H), 7.59–7.58 (m, 1H), 7.39–7.37 (m, 1H), 7.02–7.0 (d, 1H).

### Synthesis of 2

2-Aminophenylarsonic acid (217 mg, 1 mmol) and 2-hydroxy-1-naphthaldehyde (173 mg, 1 mmol) were dissolved separately in 10 mL of acetone and then mixed. The resultant solution was stirred at 70 °C for 15–20 minutes and filtered hot to yield greenish yellow crystals by slow evaporation in a day. Yield: 69.0%. M.P: 230 °C. IR, $\nu$, $cm^{-1}$: 3057, 1619, 1461, 1156, 809. Abs peaks (nm): 416. $^1$H NMR (500 MHz, DMSO-$d_6$): 12.8

(s, 1H), 9.4 (s, 1H), 8.20–8.18 (d, 1H), 7.96–7.95 (d, 2H), 7.95–7.91 (d, 1H), 7.90–7.86 (d, 1H), 7.61–7.60 (m, 2H), 7.59–7.58 (m, 1H), 7.40–7.38 (m, 1H),7.22–7.20 (d, 1H).

### Synthesis of 3

2-Aminobenzene sulfonic acid (172 mg, 1 mmol) and 2-hydroxy-1-naphthaldehyde (173 mg, 1 mmol) were dissolved separately in 10 mL of methanol/$H_2O$ and methanol, respectively, and then mixed. The resultant solution was stirred at 70 °C for 15–20 minutes and filtered hot to yield yellow-coloured crystals in 30 minutes. Yield: 70%. M.P: >250 °C. IR, $\nu$, $cm^{-1}$: 3383, 1634, 1554, 1178, 1085, 831. Abs. Peaks (nm): 414. $^1H$ NMR (500 MHz, DMSO-$d_6$): 12.50 (s, 1H), 12.38 (s, 1H), 9.44 (d, 1H), 8.81–8.80 (d, 2H), 8.29–8.28 (d, 1H), 7.93–7.91 (d, 1H), 7.86–7.85 (m, 3H), 7.60–7.5 (m, 1H), 7.40–7.38 (m, 1H), 7.22–7.21 (d, 1H).

## Results and discussion

Schiff bases **1–3** were obtained in excellent yields by refluxing the precursors in 1 : 1 v/v methanol/$H_2O$ (**1** and **3**) or acetone (**2**), in a stoichiometric ratio, followed by slow evaporation under ambient conditions, Scheme 1. Product formation was indicated by colour changes and very high melting point values: >250 °C (**1**), 230 °C (**2**), and >250 °C (**3**) of the products and further validated by other thermal and spectroscopic methods. FT-IR spectroscopic studies suggest product formation, as the key diagnostic condensation peak indicative of imine (C=N) functionality appears at 1626, 1619, and 1634 $cm^{-1}$, for **1–3**, respectively. The arsenic group's symmetric stretching frequencies are observed at 824 $cm^{-1}$ in **1** and 809 $cm^{-1}$ in **2**, while the stretching is observed at 1178 $cm^{-1}$ in **3**, for the sulfonate group, Fig. 1a. Product formation is also supported by $^1H$ NMR and HR-MS spectroscopy. Chemical shifts, peak splitting, and intensities in the $^1H$ NMR spectra of **1–3** are in agreement with their proton positions, Fig. S1–S3. Molecular mass data align precisely with the expected structures, as M+1 peaks are observed at $m/z$ values of 372, 372, and 328 for **1–3**, respectively, Fig. S4–S6. Other than early weight loss in the TGA curve of **3**, corresponding to lattice solvents, the molecular solids are very stable up to 300 °C, after which the combustion-triggered weight loss is observed, Fig. 1c.

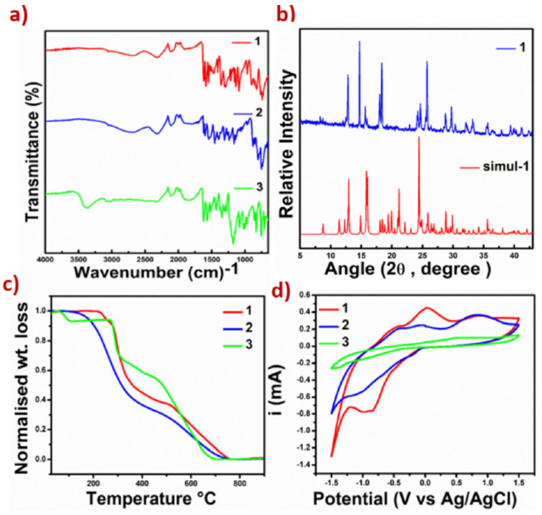

Fig. 1 (a) FT-IR spectra of **1–3**, (b) experimental and simulated P-XRD curves of **1**, (c) TGA curves of **1–3**, and (d) comparative cyclic voltammograms of **1–3** at a scan rate of 50 mV $s^{-1}$.

Powder X-ray diffraction (P-XRD) analysis of the products establishes the crystalline nature and phase purity of the molecular solid **1**, as indicated by good agreement between simulated and experimental diffraction curves, Fig. 1b. Moderate discrepancies are observed in the powder X-ray data of **2** and **3**, particularly towards higher angle values, plausibly arising from mild phase changes upon size reduction or desolvation, Fig. S7.

The electrochemical properties of the synthesized arsenic and sulfonic Schiff bases were analysed using cyclic voltammetry (CV). The cyclic-voltammograms are presented in Fig. 1(d). In order to estimate the HOMO and LUMO energy levels of the Schiff bases, the cyclic voltammetry was carried out by utilizing a three-electrode system, in which the counter electrode was a platinum wire, the reference electrode was Ag/AgCl and the working electrode was a glassy carbon electrode. All the electrochemical measurements were made at room temperature in methanol solvent and using 0.1 M $KNO_3$ as a supporting electrolyte. HOMO and LUMO energy levels can be calculated according to the following equations:

$$E(\text{HOMO}) = -e(E_{\text{ox}} + 4.4)(\text{eV}), \text{ and } E(\text{LUMO}) = -e(E_{\text{red}} + 4.4)(\text{eV})$$

where $E_{\text{ox}}$ is the onset of oxidation potential, and $E_{\text{red}}$ is the onset of reduction potential (Table S2).

### Photophysical studies

The three Schiff bases have been investigated for their optical properties in both solution and solid phases. Diffuse reflectance absorption studies of **1–3** indicate strong intermolecular charge transfer interactions within the lattice, as the absorption bands are observed beyond 400 nm. Comparable absorption shifts of **1–3** reflect a slight variation in orange colour shades, Fig. 2(a) and (b). While intramolecular charge transfer interactions in the molecules can be ruled out, as the solution phase absorption behavior of **1–3** indicates the presence of π–π* and n–π* transitions and the absence of any type of absorption beyond 400 $cm^{-1}$, Fig. S8. Tauc plots suggest HOMO LUMO values of 2.21, 2.27, and 2.23 eV for **1–3**, respectively, Fig. S9.

The solutions of products in methanol and water are not emissive while their solid-state luminescence is varied, as **1** appears yellow ($\lambda_{\max}$ = 558 nm), **2** green ($\lambda_{\max}$ = 525 nm), and **3** mustard yellow ($\lambda_{\max}$ = 535 nm), under long wavelength UV exposure, with different emission intensities, Fig. 2a and c. The solid-state absorption behaviour of the Schiff bases with different shades of brown color is comparable, Fig. 2a and b. The studies, therefore, indicate that substituent effects are more prominent for electronic properties of excited states than ground states. Also the change in the position of the functional group in **2** leads to a mild blue shifted emission wavelength ($\Delta\lambda_{\max}$ = 30 nm) with remarkably augmented intensity (nearly 3-fold), as

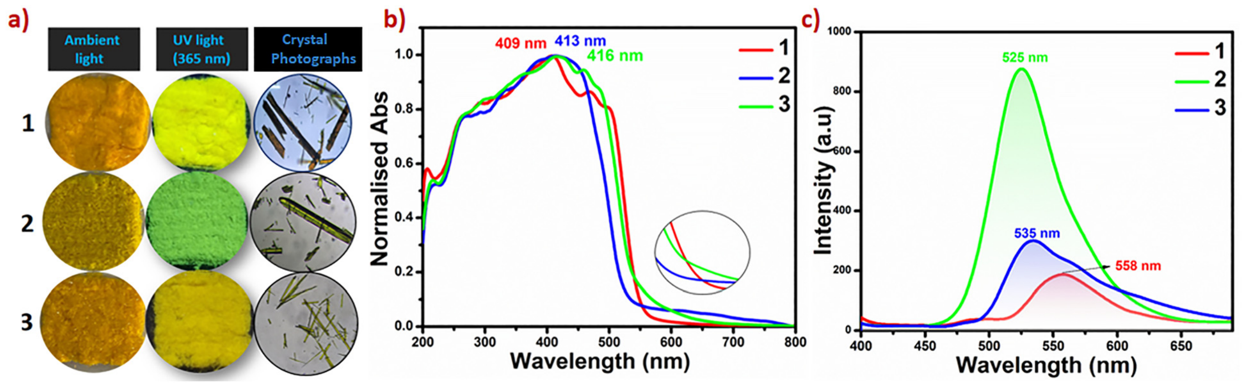

Fig. 2 (a) Digital optical images of solids **1–3** under visible and UV-light exposure and their crystal morphologies; (b) solid-phase diffuse reflectance spectra of **1–3**, measured as $BaSO_4$-diluted discs; (c) solid-state photoluminescence spectra of solids **1–3**.

compared to **1**, while changing the nature of the functional group in **3** results in notable blue-shifted emission ($\Delta\lambda_{max}$ = 23 nm) of nearly comparable intensity to that of **2**.

### Multi-stimuli responsive studies

**Mechanofluorochromism.** Mechanical stimulation can significantly alter the molecular packing of crystalline solids, resulting in optical tuning. Mechanochromic materials, which undergo color or intensity changes upon application of mechanical force, like grinding, are especially valuable for applications in sensing, data storage, and encryption due to their ease of use and rapid, visible response.[38] The Schiff bases respond to mechanical grinding, as notable luminescence fading is observed without any remarkable change in absorption and emission colors upon grinding, Fig. 3a. Solid-state photo-luminescence (PL) studies validate a decrease in emission intensity and mild blue-shifted emissions of 5–8 nm in the ground forms, Fig. 3b–d. P-XRD curves of ground forms of **1–3** indicate reduced crystallinity as the peaks broaden and their intensity decreases. For **1**, decreased crystallinity is also accompanied by phase changes, Fig. 3e–g. This tendency of a material to exhibit augmented emission intensities in crystal forms or upon crystallization has been reported as crystallisation-induced enhanced emission (CIEE), and such materials provide opportunities to design pressure detectors for anti-counterfeiting and sensing applications.

This mechano-chromic behaviour highlights the sensitivity of these materials to external mechanical stimuli and demonstrates the potential of utilizing these materials in applications that require responsive, reversible luminescence for monitoring mechanical stress or deformation.

**Thermofluorochromism.** Besides mechanical grinding, temperature is another common external factor that can influence the intermolecular interactions and molecular conformations or packing to result in modulated properties. Therefore, **1–3** have been studied for their thermofluorochromism. **1** and **3** exhibit reversible thermofluorochromism when heating at 90 °C and 100 °C, respectively, followed by ambient cooling, Fig. 4a. **2** does not undergo any chromic/fluorochromic change upon heating. Red shifted emission from yellow to brown in **1** (reverts instantaneously upon cooling) and yellow to orange ($\Delta\lambda_{max}$ = 13 nm) in **3** is notable to the visible eye and has been validated through solid-state PL studies for **3**, Fig. 4(b) and Fig. S10. Data collection for the 1H form was not possible due

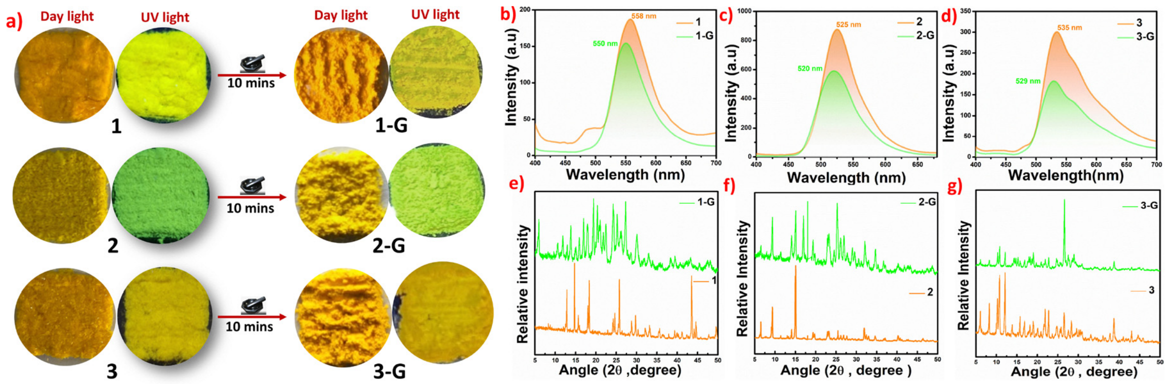

Fig. 3 (a) Digital optical images of solids **1–3** illustrating mechano-responsive luminescence switching (**1G–3G**) under visible and UV light exposure, (b–d) photoluminescence spectra of **1–3** illustrating mechano-responsive luminescence switching (**1G–3G**) and (e and f) P-XRD patterns of **1–3** vividly showcasing mechano-responsive luminescence switching (**1G–3G**).

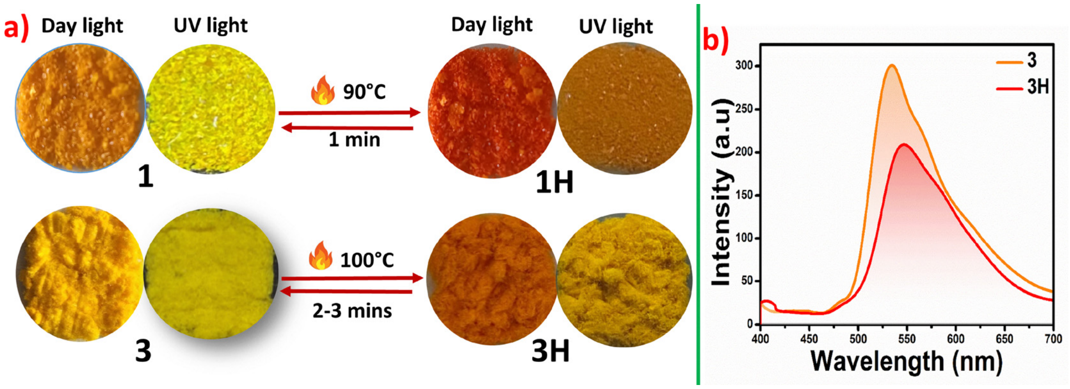

Fig. 4 (a) Digital optical images of samples **1** and **3** displaying changes in luminescence when subjected to heating, observed under both visible and ultraviolet (UV) light exposure and (b) luminescence spectra of **3** displaying changes in luminescence upon heating.

to the very fast conversion of the heated form to **1**. The explanation for thermochromism and its difference in **1–3** is provided in the Structure–property relationships section.[39,40]

**Thin film studies.** For practical applications, despite desirable optical properties, processing and integration of crystals into devices are challenging. In contrast, thin films offer a more versatile platform for device fabrication and practical utility due to their ease of handling, flexibility, and compatibility with various substrates. However, a critical limitation in the transition from bulk crystals to thin films is the potential for phase transformations upon dissolution or size reduction, which can lead to emission quenching or tuning, compromising their performance.

Therefore, we have carried out thin film studies of **1–3**, by loading the slurry of products prepared in a range of solvents, on glass slides, ensuring uniform deposition and optimal film formation (Fig. 5). The thin films were thoroughly characterized to assess their structural integrity and optical properties. It can be observed that the solid forms retain emission upon formation of films with mild (in **1**) to no change (in **2** and **3**) at emission wavelengths between the two types of solid forms, Fig. 5a–c. For **1**, the emission of crystal forms is retained in solvents like hexane and acetonitrile, while the emission is blue-shifted in other solvents by 3–23 nm, Fig. S11. Emission of crystal forms is retained in thin films of **2** in nearly all types of solvents, while thin films of **3** in all the solvents show an

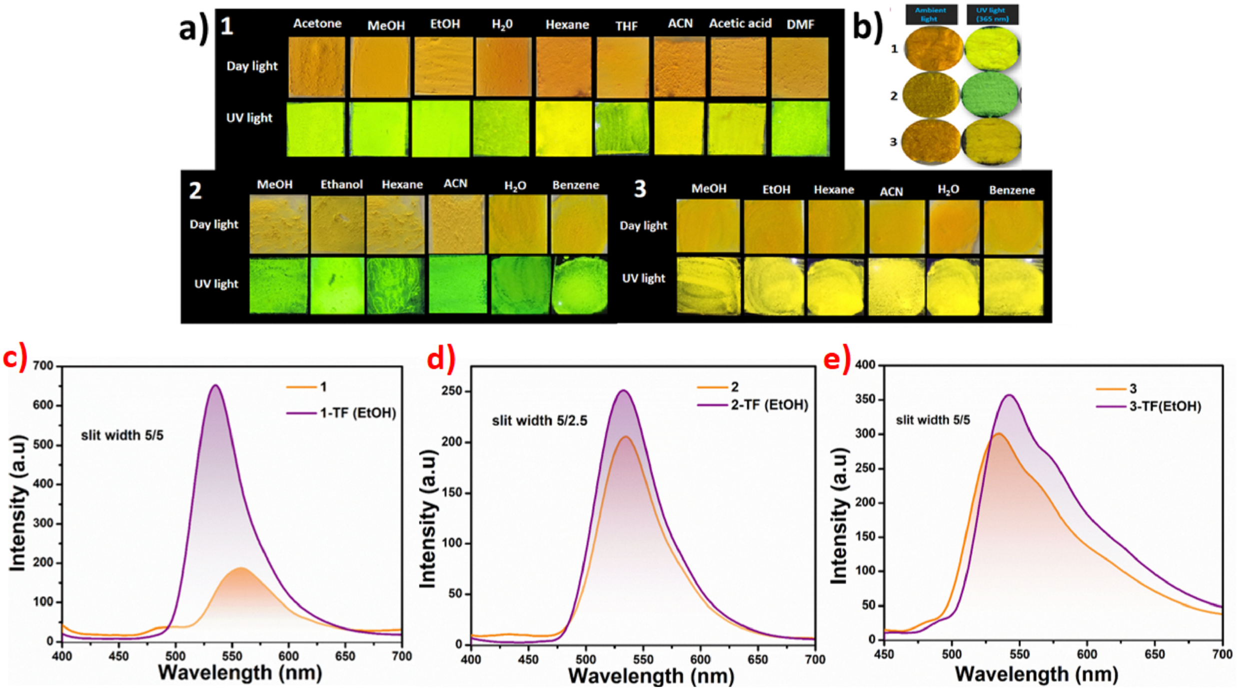

Fig. 5 (a) Optical images of thin films of **1–3** in various solvents under ambient and UV light, (b) optical images of solid forms of **1–3** under ambient and UV light, (c–e) comparative emission spectra of solid forms and thin films of **1–3**, prepared in ethanol and recorded at an excitation wavelength of 365 nm and a slit width of 5/5 nm for **1** and **3** and 5/2.5 nm for **2**, due to the very high intensity of the spectra of thin films.

insignificant red-shift of 7–11 nm, Fig. S11–S13. To our interest, the emission intensity of thin films augments strikingly in **1** and **2** compared to **3**. Unlike **1** and **3**, the emission of thin films of **2** was too intense to be in the range of the equipment at slit width values of 5/5 nm; therefore, slit width values of 5/2.5 nm were used instead of 5/5 nm used for data collection of **1** and **3**. Multi-fold enhancement in the emission intensity of thin films can be attributed to the CIEE effect; as observed in optical microscopy, the resultant thin films are composed of microcrystals of definite and uniform shapes and morphologies, Fig. S14–S17. The crystalline nature of ethanol thin films of **1–3** is also validated by powder-X-ray diffraction studies, Fig. S18–S20.

To understand the emission variation in thin films of **1** with respect to the solvent used for their preparation, their powder X-ray diffraction characterization was carried out, Fig. S21. The diffraction curves indicate phase variations, and closely related phases for green emitting films (ethanol, methanol, acetic acid, *etc.*) and nearly identical phases for yellowish films (hexane and ACN), but the two sets are very different from each other. These results validate that emission variations in thin-films of **1** arise from phase changes.

### Application in selective sensing of Zn(II) ions

Zinc is the second most abundant transition metal ion in biology, after iron. Fluorescent sensors for zinc ions have gained significant interest due to the essential roles of zinc in living organisms.[41] Therefore, monitoring of Zn(II) ions in bio-systems and the environment is essential.[42] Of the various analytical techniques used for the detection of Zn(II) ions, fluorometric detection is desirable, due to high sensitivity, selectivity, ease of observation, and practical applications in living organisms[43]

Schiff base fluorescent sensors have been extensively studied due to their ability to coordinate a range of divalent ions, making them non-selectively divalent ion sensors. We have used non-emissive methanol solutions ($10^{-3}$ M) of **2** as a probe, which upon gradual addition (up to 100 μL) of $10^{-3}$ M methanolic solution of zinc acetate undergo emission turn-on, Fig. 6b. To probe the selectivity of **2** towards Zn(II) ions, similar titrations were carried out with a range of other divalent ions: $Cr^{2+}$, $Mn^{2+}$, $Fe^{2+}$, $Co^{2+}$, $Ni^{2+}$, $Cu^{2+}$, $Cd^{+2}$, and $Hg^{2+}$. Interestingly, the emission turn-on is only observed in the case of Zn(II), establishing the selectivity, Fig. 6a and d. The limit of detection (LOD) values for Zn(II) have been calculated to be 4.9 μM, which is well below the WHO guidelines (76 μM).[44] The tabulated LOD values of some important Zn(II) sensors are provided in Table S3.[45–50] And for calculating the binding constant the Benesi–Hildebrand equation was used, yielding $K$ (binding constant) = $2.5 \times 10^3$ $M^{-1}$, Fig. S22.

Interference studies carried out in the presence of other ions, as well as Zn(II) solutions prepared in tap water, did not affect the selectivity and LOD values, Fig. 6c. Unlike **2**, **1** and **3** did not show notable sensing of Zn(II) ions. Selectivity of **2** arises due to the favourable position and nature of the functional group in **2** compared to that in **1** and **3**.

To have a further understanding of the selectivity of methanolic solution of **2** for Zn(II) ions we carried out experiments to determine the stoichiometry of the resultant complex. Job's plot obtained by continuous variation of precursors indicates complex formation between Zn(II) and **2** in 1 : 1 stoichiometry, Fig. S23. We believe the more probable configuration for this stoichiometric ratio is tetrahedral coordination about Zn(II), with three binding sites engaged by **2** and fourth by a solvent molecule, Fig. S24, as the coordination environment (both tetrahedral and octahedral) for Zn(II) in the other plausible 2 : 2 complex does not fit well. Selectivity for Zn(II) by **2** plausibly arises from the coordination tendency of the arsenate group with two acidic hydroxyl groups providing preference for relatively harder Zn(II) ions. Similarly, **3** having an *ortho*-sulfonate group with only one acidic hydroxyl moiety lacks strong affinity for Zn(II) ions.

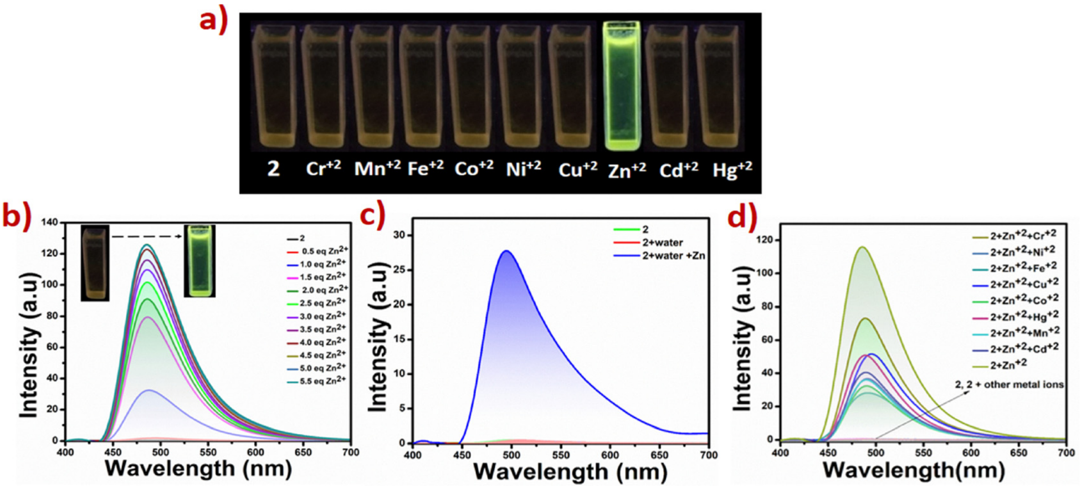

Fig. 6 Fluorochromic sensing of Zn(II) ions by a methanolic solution of **2**. (a) Images of solutions of **2** in the presence of divalent ions, highlighting selective fluorescence turn-on by Zn(II) ions, (b) fluorescence spectra obtained by titration of a $10^{-3}$ M methanolic solution of Zn(II) ions against a $10^{-3}$ M methanolic solution of **2**, (c) the interference study carried out in tap water, and (d) interference studies carried out in the presence of other divalent ions.

## Structural description

Single crystal X-ray diffraction (SC-XRD) analyses have been carried out to have further insights into the molecular packing of molecular solids **1–3**. **1** crystallizes in the monoclinic space group $P_{21/n}$ in a $Z'$ =1 form, while **2** and **3** crystallize in monoclinic $P_{21/c}$ space groups in high $Z'$ forms, with $Z'$ = 2, Fig. 6a, d and g. The molecules of **1** are nearly planar ($\varphi$ = 12.45°) and stabilised by the ionic intramolecular hydrogen bond O···H–N in the keto tautomeric form obtained by proton transfer between adjacent hydroxyl and imine centers. **2** and **3** are more non-planar than **1**, and molecular configurations are also stabilised by ionic intramolecular O···H–N interactions in all molecules present in the asymmetric unit. Interestingly, unlike in **1** and **2**, the intramolecular proton transfer to the imine nitrogen center occurs from the sulfonate group in **3**, due to the more acidic nature of **3**, preventing the scope of keto–enol tautomerism. Moreover, **3** crystallises with a water molecule and has three water molecules in ASU, plausibly due to a smaller number of acidic hydrogens in the sulfonic group ($-SO_3H$) than that in the arsenic group ($-AsO_3H_2$), in order to balance the formation of hydrogen bonds within the lattice.

The reported molecular solids form extensive hydrogen-bonded networks through arsenate and sulfonate functionalities. In **1**, two molecules of arsenate dimerise through head-to-head centrosymmetric interaction to form an $R_2^2(8)$ homo-synthon, which is extended through interaction between the second arsenic acid hydroxyl group and naphthoxide oxygens, on both ends of the synthon to form a tetrahedral growth node, Fig. 7b. The similar hydrogen-bonded pattern repeats at the arsenic acid ends of the molecules to form a 2-dimensional network solid, Fig. 7c, which associates through unusual (Ar)–C–H···As [3.917(1) Å; 161.66(1)°] interactions to form a 3-dimensional solid. The lattice is further stabilised by weak C–H···O and C–H···π interactions, while no significant π–π interactions are observed.

In **2**, the two molecules in ASU dimerise through an $R_2^2(8)$ homo-synthon, which grows on both sides of the synthon involving sulfonate groups and reproducing $R_2^2(8)$ synthons to form 1-dimensional hydrogen-bonded tapes. The tapes form an H-type π-stack on one end and slipped π–π contacts on the other end to form a 2-dimensional aggregate, Fig. 7e, which grows through C–H···O contacts into a 3-dimensional solid, Fig. 7f.

**3** crystallises with water molecules. Three sulfonate oxygens and the hydroxyl group of **3** hydrogen bond to four different water molecules to form two sets of 1-dimensional hydrogen-bonded tapes, Fig. 7h, which are further stabilised by slipped π–π aggregates. The two types of molecular tapes are held together by weak C–H···O (water) contacts to form a 3-dimensional aggregate, Fig. 7i.

## Hirshfeld studies

To further complement structural studies, computational studies in the form of Hirshfeld surfaces were studied using Crystal Explorer software to reveal the packing pattern and contribution of intermolecular interactions. Various Hirshfeld surfaces, which include $d_{\mathrm{norm}}$, curvedness, electrostatic potential (ESP) maps, and shape-index surfaces, reveal the nature, the type of contact, and also the acceptor–donor tendency in terms of potential. The Hirshfeld surface generated within a radius of 3.8 Å and calculated over $d_{\mathrm{norm}}$ provides a three-dimensional picture of close contacts in a crystal, which

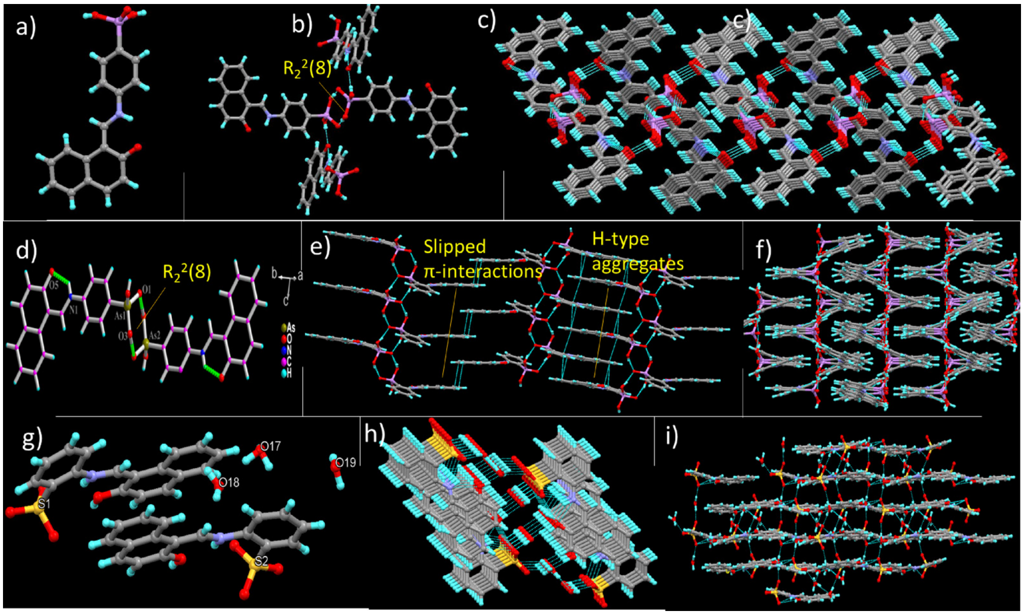

Fig. 7 Crystal structure details of **1–3**. (a) Asymmetric unit of **1**, (b) hydrogen bonded networks formed at arsenic acid groups in **1**, (c) hydrogen bonded 2-dimensional networks formed in **1**, (d) asymmetric unit of **2**, (e) association of 1-dimensional hydrogen bonded tapes through slipped π-interactions on one end and H-type aggregates on other end in **2**, (f) 3-dimensional packing arrangement of **2**, (g) asymmetric unit of **3**, (h) hydrogen bonded tapes in **3** and (i) 3-dimensional networks in **3**.

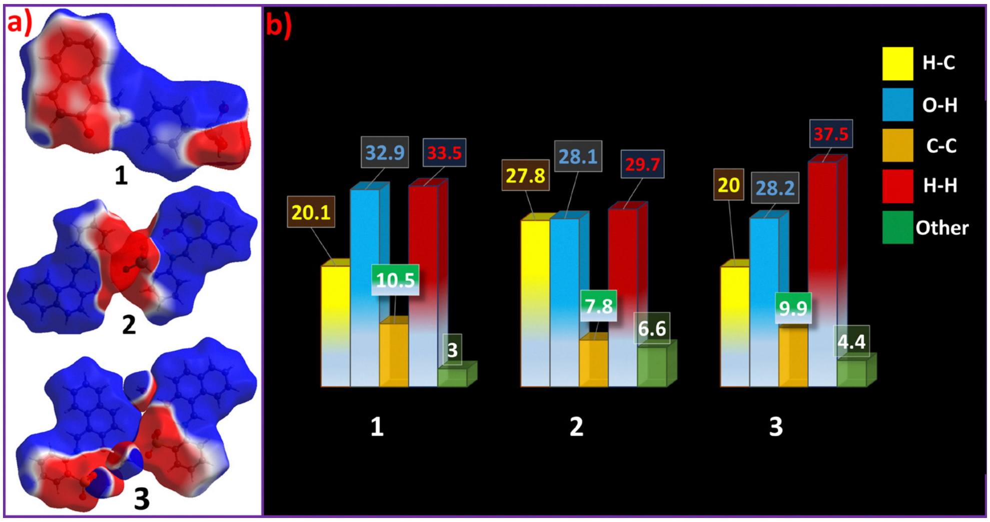

Fig. 8 (a) Electrostatic potential (ESP) maps plotted on the Hirshfeld surface of **1–3** and (b) percentage contribution of some selected intermolecular interactions in **1–3**.

can be summarized in their fingerprint plots. Hirshfeld surface properties, as well as the fingerprint plots, provide significant details of the intermolecular contacts as well as the packing of compounds **1–3**.

For compounds **1–3**, ESP maps were generated to highlight the electron-rich and electron-deficient regions, which play a crucial role in intermolecular interactions, binding affinities, and chemical reactivity. The ESP maps reveal distinct electron density variations across the molecular framework, Fig. 8a, as the naphthalene rings and arsenic acid moieties in **1** are electron-deficient regions, while for **2** and **3**, electron-deficient regions are limited around acid-functionalised regions.

The curvedness and shape index maps of **1–3** are provided as Fig. S25–S27. The fingerprint plots of solids **1–3** reveal that the primary interactions contributing to the packing of these Schiff bases are O–H/H–O, H–H, and C–H/H–C, Fig. 8b.

Interestingly, these interactions show notable variations when the functionality of the molecules is altered. The O–H/H–O interaction, for example, decreases from 32.9% in compound **1** to 28.6% in **2** and 28.2% in **3**, as the acidic functional groups are less exposed in the latter molecules for the formation of the extensive hydrogen bonding networks. Contribution of C–H···π (H–C) interactions in all three crystal forms is notable, while π–π (C–C) interactions remain relatively lower in all solid forms. Lower contribution of π–π (C–C) interactions provides a plausible explanation for the emissive nature of the solid forms. Interestingly, the luminescence intensity ratios of the solid forms are also in agreement with an inverse relation with the extent of π–π contributions, further validating that π–π interactions are responsible for emission quenching.[51]

Energy framework analysis of **1–3** has been carried out and reported, Fig. S28–S30 and Tables S4–S6. The analyses provide insights into the nature of interactions responsible for molecular packing and lattice energies.

### Structure–property relationships

Bulk properties of a material are determined by aggregation, packing, and intermolecular interactions involved. Understanding of the structure–property relationship is essential to improve the functioning of existing and design new functional materials. Optical properties, in particular, are determined by the molecular packing, as the luminescence is generally quenched by strong face-to-face π–π interactions, resulting in concentration quenching, or aggregation-induced quenching in solid forms of emissive solutions.[52,53] Therefore, design and development of solid-state emissive solids in the initial years was restricted to non-planar propeller-type molecules with a minimum scope of π-aggregation.[54] However, more recently, solid-state emission and its tuning have been observed in planar π-stacked systems with H and J-type aggregates.[55]

The reported Schiff bases **1–3** show varied solid-state emission due to a change in the position and nature of functional groups. Structural studies rule out the formation of face-to-face π-stacked dimers in the lattice of products, which is substantiated by the low contribution of C–C interactions for the molecular solids. In **1**, weak J-aggregates are observed, while slipped π–π interactions are observed in **2** and **3**, explaining their emission and its tuning in the solid state, Fig. 9d–f. Interestingly, the influence of both nature and position on emission colors is evident in **1–3**, as the emission variation between positional isomers **1** and **2**, and molecules with different functional groups at the same position, *i.e.*, **2** and **3**. The variation in emission colors in **1–3** cannot be explained based on aggregation only, as the nature and position of functional groups influence the electronic properties as well.

As the π–π interactions in crystal forms **1–3** are optimum for solid state emission resulting in CIEE, the grinding involving crushing of crystals under anisotropic force may result in

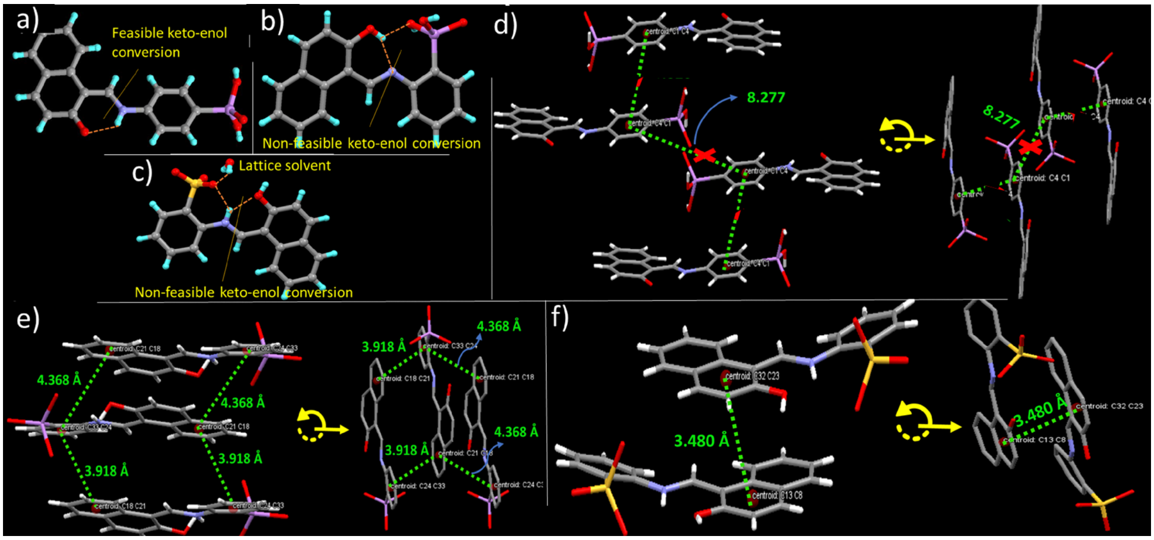

Fig. 9 Structure–property correlation in **1–3**. Structures of molecules of **1** (a), **2** (b) and **3** (c), highlighting the intramolecular hydrogen bonding and position of acidic protons or presence of lattice solvent resulting in thermochromism. Molecular packing fragments highlighting the absence of π–π interactions or formation of H and J-type aggregates in **1** (d), **2** (e) and **3** (f).

disruption of long-range π-interactions leading to decreased emission intensities.

Of the three products, only **1** and **3** show thermofluorochromism at 90 °C and 100 °C, respectively. The phenomenon under ambient conditions is reversible and very fast in **1** compared to that in **3**, as the former reverts back in less than a minute, while the latter takes around three minutes. Very fast reversion of **1** limits characterization of its heated form; however, based on structural studies, different mechanisms are attributed to the phenomenon in **1** and **3**. Unlike **3**, **1** does not undergo proton transfer between arsenic acid and the imine centre, instead it can exhibit keto–enol tautomerism due to transfer of adjacent hydroxyl protons to the imine centre, Fig. 9a, while keto–enol tautomerism is prevented in **3** due to the transfer of the sulfonate proton to the imine centre, Fig. 9c. Very fast reversible thermochromism in **1** can therefore be attributed to the tautomerism, as it has a planar configuration, $\phi = 12.45°$, and a free cell volume ($V_{\text{free}}$) of 92.88 Å$^3$, suitable for the phenomenon,[56] Fig. S31. Unfortunately limited stability of 1H form limits validation of the proposed mechanism. The same mechanism cannot be extended to **3**, due to the slow reversion rate and no scope for keto–enol tautomerism. Thermochromism in **3** instead plausibly arises due to desorption and reabsorption of lattice water molecules, present in its structure, Fig. 9c, as the FT-IR and TGA data of **3H** indicate loss of lattice water molecules, which is recovered upon cooling, Fig. S32 and S33. This has further been validated by allowing **3H** form to cool under anhydrous conditions, created by storing it in a vail packed with activated silica. In the anhydrous vial the sample retained its actual color for more than two months, Fig. S34.[56] The absence of thermochromism in **2** may be due to involvement of en-ol protons in hydrogen bonding with the adjacent arsenic acid group and the absence of water molecules in its lattice, Fig. 9b.

## Conclusion

Three luminescent Schiff bases have been synthesized, characterized, and studied for their optical properties. Emission variation has been realized through a change in the nature and position of functional groups, and structural studies attribute solid-state emission to the absence of face-to-face π-stacking interactions in the crystal lattice of the products. Mechano-chromic studies indicate decreased emission intensity upon grinding, which is attributed to loss of crystallinity upon grinding, possibly promoting π–π interactions between the molecules. The improved intensity of emission in crystalline form, *i.e.*, CIEE, is also supported by thin film studies, as the thin films prepared in a range of solvents show a striking increase in the emission intensities recorded for the thin film forms, attributed to the formation of uniform microcrystals. Stimuli-responsive studies indicate reversible thermofluorochromism in **1** and **3**, with instantaneous reversal in **1**, compared to slow reversal in **3**, The difference in the thermo-fluorochromic behaviour is attributed to keto–enol prototropism in **1** and breathing of lattice water in **3**. Methanolic solution of **2** shows selective sensing of Zn(II) with an LOD value of 4.9 μM, and a suitable explanation for discriminatory sensing of Zn(II) by only **2** is provided. The studies represent an intriguing case to understand the structure–property relationships and provide a way forward for the design of photonic crystals of simple molecules.

## Conflicts of interest

There are no conflicts to declare

## Data availability

The data supporting this article have been included as part of the supplementary information (SI). Supplementary information: NMR, hydrogen bonding parameters, Hirshfeld surfaces, crystal structure diagrams, solution phase studies, and zinc sensing. See DOI: https://doi.org/10.1039/d5ma01080b.

CCDC 2444241–2444243 contain the supplementary crystallographic data for this paper.[57a–c]

## Acknowledgements

A. D. acknowledges DST-SERB, New Delhi, for funding under the Core Research Grant (CRG/2022/003693). S. F. is thankful to CSIR New Delhi for providing funds under project No. 09/0251(24505)/2025-EMR-I. S. F. and I. A. thank the Department of Chemistry and the University of Kashmir for the support and facilities.

## Notes and references

1 K. W. Lee, Y. Wan, Z. Huang, Q. Zhao, S. Li and C. S. Lee, Organic optoelectronic materials: A rising star of bioimaging and phototherapy, *Adv. Mater.*, 2024, **36**(17), 2306492.
2 X. Song, X. Wang, W. Liu, X. Chen, S. Li, M. S. Islam, L. Li, X. Zhao, C. Redshaw and Y. Zhao, Organic Photo-Responsive Piezoelectric Materials Based on Pyrene Molecules for Flexible Sensors, *Adv. Electron. Mater.*, 2025, 2400933.
3 Z. Miao, C. Gao, H. Gao, Z. Qin, W. Hu and H. Dong, High-Efficiency Area-Emissive White Organic Light-Emitting Transistor for Full-Color Display, *Adv. Mater.*, 2024, **36**(1), 2306725.
4 X. Wang, Z. Wang, X. Wang, F. Kang, Q. Gu and Q. Zhang, Recent Advances of Organic Cocrystals in Emerging Cutting-Edge Properties and Applications, *Angew. Chem., Int. Ed.*, 2024, **136**(51), e202416181.
5 Z. Wu, H. Choi and Z. M. Hudson, Achieving White-Light Emission Using Organic Persistent Room Temperature Phosphorescence, *Angew. Chem., Int. Ed.*, 2023, **135**(32), e202301186.
6 I. Ahmad and A. A. Dar, Switching the Solid-State Emission of Organic Crystals through Coformer Choice and Vapochromism, *J. Phys. Chem. C*, 2023, **127**(37), 18684–18693.
7 A. A. Ahangar, A. A. Malik, I. Ahmad and A. A. Dar, Mechanistic insights into the aggregation-induced emission of halogenated Schiff base fluorescent probes, *Dyes Pigm.*, 2023, **220**, 111742.
8 I. Ahmad, A. A. Malik, S. Ahmad and A. A. Dar, Sulfonate–Pyridinium Ionic Cocrystal Solvates: Improved Material and Antimicrobial Properties, *Cryst. GrowthDes.*, 2024, **24**(11), 4790–4800.
9 D. Barman, M. Annadhasan, A. P. Bidkar, P. Rajamalli, D. Barman, S. S. Ghosh, R. Chandrasekar and P. K. Iyer, Highly efficient color-tunable organic co-crystals unveiling polymorphism, isomerism, delayed fluorescence for optical waveguides and cell-imaging, *Nat. Commun.*, 2023, **14**(1), 6648.
10 S. Guieu, F. Cardona, J. Rocha and A. M. Silva, Tunable Color of Aggregation-Induced Emission Enhancement in a Family of Hydrogen-Bonded Azines and Schiff Bases, *Chem. – Eur. J.*, 2018, **24**(65), 17262–17267.
11 P. Nitschke, B. Jarzabek, A.-E. Bejan and M.-D. Damaceanu, Effect of protonation on optical and electrochemical properties of thiophene–phenylene-based Schiff bases with alkoxy side groups, *J. Phys. Chem. B*, 2021, **125**(30), 8588–8600.
12 A. K. Satapathy, S. K. Behera, A. Yadav, L. N. Mahour, C. Yelamaggad, K. Sandhya and B. Sahoo, Tuning the fluorescence behavior of liquid crystal molecules containing Schiff-base: Effect of solvent polarity, *J. Lumin.*, 2019, **210**, 371–375.
13 W. Wang, L. Luo, P. Sheng, J. Zhang and Q. Zhang, Multifunctional features of organic charge-transfer complexes: advances and perspectives, *Chem. – Eur. J.*, 2021, **27**(2), 464–490.
14 L. Sun, W. Zhu, X. Zhang, L. Li, H. Dong and W. Hu, Creating organic functional materials beyond chemical bond synthesis by organic cocrystal engineering, *J. Am. Chem. Soc.*, 2021, **143**(46), 19243–19256.
15 J. Song, H. Liu, Z. Zhao, P. Lin and F. Yan, Flexible organic transistors for biosensing: devices and applications, *Adv. Mater.*, 2024, **36**(20), 2300034.
16 S. Chang, J. H. Koo, J. Yoo, M. S. Kim, M. K. Choi, D.-H. Kim and Y. M. Song, Flexible and stretchable light-emitting diodes and photodetectors for human-centric optoelectronics, *Chem. Rev.*, 2024, **124**(3), 768–859.
17 F. Wang, D. Liu, J. Li and M. Ma, Molecular Engineering of Host Materials for High-Performance Phosphorescent OLEDs: Zig-Zag Conformation with 3D Gridding Packing Mode Facilitating Charge Balance and Quench Suppression, *Adv. Funct. Mater.*, 2018, **28**(39), 1803193.
18 M. D. Malla, A. A. Malik, A. A. Ahangar, S. Dey, N. Sharma, D. A. Jose, D. Chopra and A. A. Dar, Design of AIE-active Schiff-bases: Mechanochromic, Thermochromic and Sensing Studies, *Chem. Select*, 2024, **9**(44), e202404488.
19 I. Ahmad, A. A. Malik and A. A. Dar, Multi-Stimuli-Responsive Organo-Sulfonated Anil and Its Organic Complex, *Cryst. GrowthDes.*, 2022, **22**(11), 6483–6492.
20 W. Wang, Y. Zhou, L. Yang, X. Yang, Y. Yao, Y. Meng and B. Tang, Stimulus-responsive photonic crystals for advanced security, *Adv. Funct. Mater.*, 2022, **32**(40), 2204744.
21 Y. Huang, L. Ning, X. Zhang, Q. Zhou, Q. Gong and Q. Zhang, Stimuli-fluorochromic smart organic materials, *Chem. Soc. Rev.*, 2024, **53**(3), 1090–1166.
22 H. Ye, G. Liu, S. Liu, D. Casanova, X. Ye, X. Tao, Q. Zhang and Q. Xiong, Molecular-barrier-enhanced aromatic fluorophores in cocrystals with unity quantum efficiency, *Angew. Chem.*, 2018, **130**(7), 1946–1950.
23 Z. Wang, F. Yu, W. Chen, J. Wang, J. Liu, C. Yao, J. Zhao, H. Dong, W. Hu and Q. Zhang, Rational control of charge transfer excitons toward high-contrast reversible mechanoresponsive luminescent switching, *Angew. Chem., Int. Ed.*, 2020, **59**(40), 17580–17586.

24 I. Ahmad, A. A. Ganie, S. Ahmad, A. A. Ahangar, C. M. Reddy and A. A. Dar, A high Z′ structure of an organic salt with unusually high phase stability, nanoindentation, and mechano and vapo-fluorochromism, *CrystEngComm*, 2023, **25**(21), 3164–3170.

25 S. P. Anthony, Organic solid-state fluorescence: strategies for generating switchable and tunable fluorescent materials, *ChemPlusChem*, 2012, **77**(7), 518–531.

26 A. A. Dar, S. H. Lone, I. Ahmad, A. A. Ahangar, A. A. Ganie and C. Femina, Engineering the solid-state luminescence of organic crystals and cocrystals, *Mater. Adv.*, 2024, **5**(3), 1056–1064.

27 A. A. Malik, Z. M. Saeed, I. Ahmad, T. Alkhidir, P. B. Managutti, S. Mohamed and A. A. Dar, Polymorphism Steered Thermochromism in a Sulfonamide, *ACS Appl. Opt. Mater.*, 2024, **2**(8), 1709–1720.

28 C. Wei, L. Li, Y. Zheng, L. Wang, J. Ma, M. Xu, J. Lin, L. Xie, P. Naumov and X. Ding, Flexible molecular crystals for optoelectronic applications, *Chem. Soc. Rev.*, 2024, **53**(8), 3687–3713.

29 A. A. Dar and A. A. Malik, Photoluminescent organic crystals and co-crystals, *J. Mater. Chem. C*, 2024, **12**(27), 9888–9913.

30 Y. Ye, Y. Sun, Y. Zhang, G. Ding, H. Hao, Y. Zhang and C. Xie, 2D Elastic Organic Crystals with Thermomechanical/Acid Responses and Dual-Mode Optical Waveguides, *Adv. Opt. Mater.*, 2024, **12**(21), 2400539.

31 L. Lan, L. Li, P. E. Naumov and H. Zhang, Flexible organic crystals for dynamic optical transmission, *Chem. Mater.*, 2023, **35**(18), 7363–7385.

32 W. M. Awad, D. W. Davies, D. Kitagawa, J. M. Halabi, M. B. Al-Handawi, I. Tahir, F. Tong, G. Campillo-Alvarado, A. G. Shtukenberg and T. Alkhidir, Mechanical properties and peculiarities of molecular crystals, *Chem. Soc. Rev.*, 2023, **52**(9), 3098–3169.

33 N. P. Thekkeppat, M. Lakshmipathi, A. S. Jalilov, P. Das, A. M. P. Peedikakkal and S. Ghosh, Combining optical properties with flexibility in halogen-substituted benzothiazole crystals, *Cryst. GrowthDes.*, 2020, **20**(6), 3937–3943.

34 T. Feiler, B. Bhattacharya, A. A. Michalchuk, S.-Y. Rhim, V. Schröder, E. List-Kratochvil and F. Emmerling, Tuning the mechanical flexibility of organic molecular crystals by polymorphism for flexible optical waveguides, *CrystEngComm*, 2021, **23**(34), 5815–5825.

35 A. A. Dar, A. A. Ahangar, C. Femina, A. A. Malik, J. V. Parambil and P. K. Sajith, Combined Experimental and Theoretical Investigations of a Photoswitching Dimorphic Chlorinated Schiff Base, *J. Phys. Chem. C*, 2024, **128**(44), 18901–18912.

36 A. A. Ahangar, A. A. Malik, S. Ahmad and A. A. Dar, Halogenated Anils of Sulfanilamide: Structural, Hirshfeld, and Optical Studies, *Chem. Select*, 2024, **9**(46), e202402872.

37 I. Ahmad, A. A. Dar and S. J. Prathapa, Photo-switching in the multi-stimuli responsive low Z'-high Z'co-crystal polymorphs, *J. Mater. Chem. C*, 2025, **13**(23), 6264–6271.

38 Y. Hu, C. Qi, D. Ma, D. Yang and S. Huang, Multicolor recordable and erasable photonic crystals based on on-off thermoswitchable mechanochromism toward inkless rewritable paper, *Nat. Commun.*, 2024, **15**(1), 5643.

39 M. Rauf, S. Hisaindee and N. Saleh, Spectroscopic studies of keto–enol tautomeric equilibrium of azo dyes, *RSC Adv.*, 2015, **5**(23), 18097–18110.

40 A. A. Dar and A. A. Ganie, Irreversible Thermochromism in organic salts of sulfonated Anils, *Cryst. GrowthDes.*, 2020, **20**(6), 3888–3897.

41 K. P. Carter, A. M. Young and A. E. Palmer, Fluorescent sensors for measuring metal ions in living systems, *Chem. Rev.*, 2014, **114**(8), 4564–4601.

42 Y. Zhang, Y. Zhao, Y. Wu, A. Zhou, Q. Qu, X. Zhang, B. Song, K. Liu, R. Xiong and C. Huang, Well-defined organic fluorescent nanomaterials with AIE characteristics for colorimetric/UV-vis/fluorescent multi-channel recognition of Zn 2+ with multiple applications in plant cells and zebrafish, *Mater. Chem. Front.*, 2021, **5**(13), 4981–4988.

43 A. K. R. Ahmed, R. Gajendhiran, S. Mithra, S. A. Majeed, A. S. S. Hameed, R. Paulpandiyan, S. Maniyammai, G. T. S. Andavan, M. NizamMohideen and A. K. Rahiman, Salicylidene-based dual-responsive 'turn on' fluorometric chemosensors for the selective detection of Zn 2+, Al 3+ and F− ions: theoretical investigation and applications in the live cell imaging of zebrafish larvae and molecular logic gate operation, *J. Mater. Chem. B*, 2025, **13**(2), 622–641.

44 S. A. El-Safty, M. Shenashen, M. Ismael, M. Khairy and M. R. Awual, Optical mesosensors for monitoring and removal of ultra-trace concentration of Zn (II) and Cu (II) ions from water, *Analyst*, 2012, **137**(22), 5278–5290.

45 D. Yun, J. B. Chae, H. So, H. Lee, K.-T. Kim and C. Kim, Sensing of zinc ions and sulfide using a highly practical and water-soluble fluorescent sensor: applications in test kits and zebrafish, *New J. Chem.*, 2020, **44**(2), 442–449.

46 S. Enbanathan, S. Munusamy, D. Jothi, S. Manojkumar, S. Manickam and S. K. Iyer, Zinc ion detection using a benzothiazole-based highly selective fluorescence ''turn-on'' chemosensor and its real-time application, *RSC Adv.*, 2022, **12**(43), 27839–27845.

47 B. Das, M. Dolai, A. Dhara, S. Mabhai, A. Jana, S. Dey and A. Misra, Acetate ion augmented fluorescence sensing of Zn2+ by Salen-based probe, AIE character, and application for picric acid detection, *Anal. Sci. Adv.*, 2021, **2**(9–10), 447–463.

48 X.-J. Bai, J. Ren, J. Zhou and Z.-B. Song, A 'turn-on' fluorescent chemosensor for the detection of Zn2+ ion based on 2-(quinolin-2-yl) quinazolin-4 (3 H)-one, *Heterocyclic Commun.*, 2018, **24**(3), 135–139.

49 B. K. Rani and S. A. John, A highly selective turn-on fluorescent chemosensor for detecting zinc ions in living cells using symmetrical pyrene system, *J. Photochem. Photobiol., A*, 2021, **418**, 113372.

50 J. M. Jung, J. J. Lee, E. Nam, M. H. Lim, C. Kim and R. G. Harrison, A zinc fluorescent sensor used to detect mercury (II) and hydrosulfide, *Spectrochim. Acta, Part A*, 2017, **178**, 203–211.

51 S. Parvarinezhad and M. Salehi, Synthesis, characterization, crystal structures, Hirshfeld surface analysis and DFT

computational studies of new Schiff Bases derived from Phenylhydrazine, *J. Mol. Struct.*, 2020, **1222**, 128780.

52 X. Feng, X. Wang, C. Redshaw and B. Z. Tang, Aggregation behaviour of pyrene-based luminescent materials, from molecular design and optical properties to application, *Chem. Soc. Rev.*, 2023, **52**(19), 6715–6753.

53 A. A. Ganie, A. A. Ahangar, A. Dhir, A. K. Gupta and A. A. Dar, Hetero-aggregation-induced tunable emission in multicomponent crystals, *J. Phys. Chem. C*, 2023, **127**(19), 9257–9267.

54 X. He and P. Wei, Recent advances in tunable solid-state emission based on α-cyanodiarylethenes: from molecular packing regulation to functional development, *Chem. Soc. Rev.*, 2024, **53**, 6636, DOI: 10.1039/D4CS00325J.

55 P. Majumdar, F. Tharammal, J. Gierschner and S. Varghese, Tuning Solid-State Luminescence in Conjugated Organic Materials: Control of Excitonic and Excimeric Contributions through π Stacking and Halogen Bond Driven Self-Assembly, *ChemPhysChem*, 2020, **21**(7), 616–624.

56 A. A. Ganie and A. A. Dar, Water Switched Reversible Thermochromism in Organic Salt of Sulfonated Anil, *Cryst. Growth Des.*, 2021, **21**(5), 3014–3023.

57 (*a*) CCDC 2444241: Experimental Crystal Structure Determination, 2025, DOI: 10.5517/ccdc.csd.cc2n1fhn; (*b*) CCDC 2444242: Experimental Crystal Structure Determination, 2025, DOI: 10.5517/ccdc.csd.cc2n1fjp; (*c*) CCDC 2444243: Experimental Crystal Structure Determination, 2025, DOI: 10.5517/ccdc.csd.cc2n1fkq.